PERGAMON

Journal of Structural Geology 23 (2001) 11–23

JOURNAL OF STRUCTURAL GEOLOGY

www.elsevier.nl/locate/jstrugeo

Initiation and reactivation of faults during movement over a thrust-fault ramp: numerical mechanical models

S. Gregg Erickson*,†, Luther M. Strayer‡, John Suppe

Princeton 3D Structure Project, Department of Geosciences, Princeton University, Princeton, NJ 08544-1003, USA

Received 5 November 1999; accepted 1 June 2000

Abstract

With numerical continuum models, we investigate the effects of fault geometry, fault friction, material properties and anisotropy on the initiation and reactivation of faults in the hanging wall of a thrust-fault ramp. The models use an elastic–plastic, frictional, dilatant, cohesion-softening material, in which deformation may localize as shear bands. With a sharp lower fault bend, backthrust shear bands propagate up from the concentration of differential stress at the fault bend. With a rounded lower fault bend, bedding-parallel shear bands develop above the fault bend in the center of the layer, where differential stress is highest. Friction on the ramp enhances the development of backthrusts, and causes them to initiate at shallower dips. Increased overburden decreases the amount of localization within shear bands and the spacing between them. Shear bands that develop at the lower fault bend are weaker than the surrounding material and are thus potential sites of reactivation during subsequent deformation. Because of this potential reactivation, the style of deformation at the upper fault bend depends on the deformation that accumulates at the lower fault bend. At the upper fault bend, backthrusts are reactivated as extension faults, and are crosscut by more steeply dipping extension faults. Bedding-parallel shear bands are reactivated at the upper fault bend with top-to-the-hinterland sense of shear. Low-angle extension faults are listric into the reactivated bedding-parallel shear bands, producing hinterland-verging extensional duplexes above the upper flat.

1. Introduction

Hanging-wall anticlines develop as a result of the ramp-flat trajectories of thrust faults (Rich, 1934; Suppe, 1983). When material moves over a thrust-fault ramp, it must deform to accommodate movement over the lower and upper fault bends, which connect the ramp to the lower and upper flats, respectively. Material moving over a ramp undergoes multiple stages of deformation as it passes through very different local states of stress adjacent to the ramp (Wiltschko, 1979; Berger and Johnson, 1982; Kilsdonk and Fletcher, 1989), and fracture, cataclasis and small-scale faulting are concentrated above fault bends (Erickson and Jamison, 1995). At the lower fault bend, material undergoes layer-parallel shortening and top-to-the-foreland shear, whereas at the upper fault bend, it undergoes layer-parallel extension and top-to-the-hinterland shear. Deformation at the lower fault bend may be accommodated either by backthrusting or by bedding-parallel slip (Serra, 1977). Bedding-surface slip is a common process in rocks as they move over a ramp (Wiltschko et al., 1985; Kilsdonk and Wiltschko, 1988). Backthrusts develop in physical models of thrust-fault ramps (Morse, 1977, 1978; Chester et al., 1991; Merle and Abidi, 1995) and also in natural structures (Jacobeen and Kanes, 1974; Serra, 1977; Spang et al., 1981; Jamison and Pope, 1996). Bedding-surface slip dominates in anisotropic rocks, whereas backthrusting is more likely in thick, isotropic sequences (Chester et al., 1991). In addition to anisotropy, other material properties, as well as fault geometry and fault friction, determine which of these mechanisms dominates.

Kinematic models of structures in thrust belts (Suppe, 1983; Jamison, 1987) rely on geometrical assumptions of deformation (e.g. layer-parallel shear of constant-thickness layers) and contain no material properties as part of the formulation. Analytical models of deformation at thrust-fault ramps (Wiltschko, 1979; Berger and Johnson, 1980, 1982; Kilsdonk and Fletcher, 1989; Chester and Fletcher, 1997) are restricted to relatively simple material properties (e.g. homogeneous linear viscosity, either isotropic or anistropic) in order to obtain a tractable solution. Physical models of rock layers deformed under confining pressure

* Corresponding author.
E-mail address: ericksonsg@appstate.edu (S.G. Erickson).
† Current address: Department of Geology, Appalachian State University, Boone, NC 28608-2067 USA.
‡ Current address: Department of Geology, California State University, Hayward, CA 94542 USA

0191-8141/01/$ - see front matter
PII: S0191-8141(00)00074-2

(Morse, 1977; Chester et al., 1991) simulate elastic–plastic, frictional, dilatant deformation at thrust-fault ramps, although they are not scaled. With numerical methods, it is possible to investigate more complex and more realistic material properties and mechanical behaviors. Numerical models of deformation at thrust-fault ramps have used viscous–plastic (Erickson and Jamison, 1995) or elastic–plastic (Strayer and Hudleston, 1997) properties. In numerical models that use an elastic–plastic, frictional, dilatant material, deformation may localize in shear bands, which simulate faults (Cundall, 1989; Ord, 1991). With these material properties, two orientations of localized shear bands, backthrust and bedding-parallel, develop above a ramp (Strayer and Hudleston, 1997). With a fine numerical grid and an elastic–plastic material that undergoes cohesion softening with increasing plastic strain, this localization of strain into shear bands can be investigated in greater detail. Using these material properties, Erickson et al. (2000) investigate mechanisms of hinge migration (backthrusting and bedding-parallel shear) during fold growth. In these numerical models, rounded fault bends and hanging-wall anisotropy both enhance bedding-parallel shear bands, whereas backthrusts develop with sharp fault bends and an isotropic material. In this paper, we investigate the deformation in an elastic–plastic, cohesion-softening material as it moves over both lower and upper fault bends of a ramp. Because of the cohesion softening, the highly-strained material within shear bands is weaker than the surrounding material. Shear bands that develop at a lower fault bend, whether backthrust or bedding-parallel, are likely sites for reactivation during movement over the upper fault bend. Thus, deformation at the upper fault bend depends on the deformation that accumulates at the lower fault bend. We investigate how structures that develop at the lower fault bend affect deformation at the upper fault bend, and whether they are reactivated or crosscut by ensuing deformation. Whether or not a shear band becomes reactivated depends on its strength relative to the surrounding material as well as its orientation relative to the local state of stress at the upper fault bend. We investigate the effects of fault geometry, fault friction and overburden on the initiation and reactivation of shear bands in the hanging wall of a thrust-fault ramp.

2. Method

We use the software FLAC (Fast Lagrangian Analysis of Continua) (Cundall and Board 1988; Coetzee et al., 1995), a two-dimensional, explicit finite-difference code, which has been used to model geologic structures (Riley, 1996; Strayer and Hudleston, 1997, Erickson et al., 2000). The explicit finite-difference method differs from finite-element methods in that gridpoints are numerically associated only with their immediate neighbors. There is no global stiffness matrix to invert, making it computationally faster than other methods. However, with the finite-difference method, time steps must be small enough to ensure numerical convergence (Cundall and Board, 1988). Coordinate positions are updated using displacements calculated from the previous time-step, and the grid is displaced along with the material it represents. Because the dynamic equations of motion are included in the formulation, the numerical scheme is stable, even if unstable physical processes are modeled. The simulations are quasistatic; kinetic energy is both generated and dissipated.

The mechanical behavior of the material is elastic–plastic. For the constitutive rule, we use Mohr–Coulomb plasticity, which consists of a yield function and a plastic flow rule. The yield function, f, which governs the onset of plastic behavior, is

$$f = \tau + \sigma\sin\phi - C\cos\phi \quad (1)$$

where τ is the maximum shear stress, σ the mean stress, ϕ the internal friction angle and C the cohesion. The plastic potential function, g, which governs plastic flow, is

$$g = \tau + \sigma\sin\psi - C\cos\psi \quad (2)$$

where ψ is the dilation angle. The dilation angle is the ratio of the plastic volume change over the plastic shear strain (Vermeer and de Borst, 1984), and is positive for a volume increase with increasing plastic shear strain. The values of cohesion, internal friction angle and dilation angle may harden or soften (increase or decrease) as a function of increasing plastic shear strain. Unequal friction and dilation angles result in non-associated plasticity, where the plastic flow rule (Eq. 2), is not associated with the yield function (Eq. 1) (Vermeer and de Borst, 1984). For upper crustal geologic materials, in which plastic behavior is both pressure-dependent and dilatant, values of the dilation angle generally are less than those of the friction angle (Cundall, 1990) and are between 10 and 20° (Vermeer and de Borst, 1984).

With non-associated plasticity, localization of deformation is possible (Cundall, 1989; Hobbs and Ord, 1989). Due to bifurcation in the governing equations, strain may be accommodated either by distributed deformation or by initiation of shear bands. Localization may occur even without a strain-softening constitutive relation, provided that the dilation angle ψ is less than the internal friction angle ϕ (Rudnicki and Rice, 1975; Vardoulakis, 1980). Localization is grid dependent; in order for a shear band to develop, the grid must be fine relative to the shear-band thickness. Shear-band localization occurs partly due to the use of the dynamic equations of motion; shear-band formation releases strain energy, which is dissipated in a physically realistic way. Localization of deformation into shear bands simulates upper-crustal faulting. However, the development of a shear band does not introduce any discontinuity into the numerical model; all initially continuous regions remain continuous throughout a simulation. In addition to the localized shear bands that may develop within the continuum, discrete interfaces, along which slip occurs, may be built

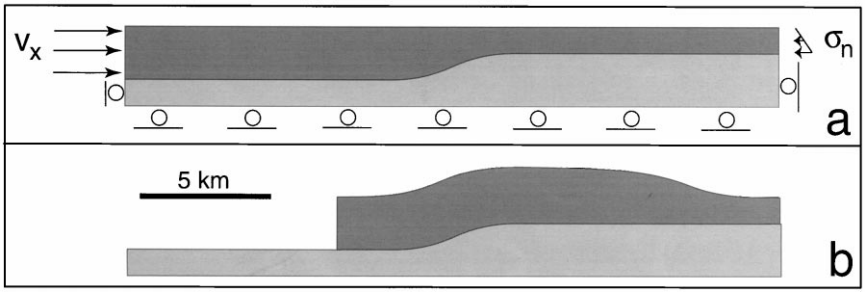

Fig. 1. (a) Model geometry and boundary conditions. A velocity boundary condition is applied to the left side of the hanging wall. A normal stress on the right side of the model, which increases linearly downward, balances gravitationally-induced stresses. The top surface is stress-free or, in some models, has a normal stress equivalent to 3 or 6 km overburden. The footwall has zero horizontal velocity on the sides and zero vertical velocity on the bottom. (b) Final geometry. Elements on the right side of the hanging wall are progressively deleted as they reach the right edge of the footwall.

into the model. These interfaces, which represent faults and bedding surfaces, are assigned normal and shear stiffnesses and a coefficient of sliding friction.

The material properties we use for the hanging wall are elastic shear modulus $G = 2.1$ GPa, elastic bulk modulus $K = 2.1$ GPa, density $\rho = 2600$ kg/m^3, initial cohesion $C = 23$ MPa, softening linearly to 11.5 MPa at an equivalent plastic strain of 0.2, friction angle $\phi = 23°$, and dilation angle $\psi = 11°$. These properties are based on experimental values of Edmond and Paterson (1972), averaged over all of the tabulated values for Carrara Marble at 100 MPa (Ord, 1991), although the cohesion is ~50% weaker than experimental values. Reduced strength properties are generally necessary to produce realistic large-scale structures in numerical mechanical models (Schultz, 1996) and are to be expected when scaling properties derived from centimeter-scale experiments to kilometer-scale geological structures. Although it would be possible to model the hardening and softening behaviors of cohesion, friction, and dilation based on experimental results in an attempt to be realistic (e.g. Ord, 1991), we have chosen to use a simple softening rule. The only softening behavior we present is a linear softening relationship for cohesion with increasing plastic strain, although tests with more complicated material behaviors give similar results.

The models are plane strain and have a geometry that consists of a hanging wall with elastic–plastic material properties and a footwall with elastic properties. The hanging wall is moved over the footwall by a constant horizontal velocity of 2 cm per time step, applied at the left side of the hanging wall, for a total displacement of 8 km (Fig. 1). At the right side of the model, hanging-wall elements are deleted as they reach the right edge of the footwall. The model is 25 km long, and the hanging wall is initially 2 km thick above the lower flat and 1 km thick above the upper flat. Hanging-wall elements are 50 m on a side, and there are approximately 15,000 elements in each model. A gravitational body force is applied to each element. In most models the top surface is stress-free, although in some models an overburden of 3 km or 6 km is simulated by applying a normal traction of 76.5 MPa or 133 MPa to the top of the model. The fault between the hanging wall and footwall has a flat–ramp–flat trajectory consisting of horizontal upper and lower flats and a ramp 1 km in height with 25° dip. In most models, the fault is a frictionless interface ($\mu = 0$), although in one set of models there is friction ($\mu = 0.36$) along the ramp. The fault bends separating flats and ramp are either sharp or rounded (Figs. 2 and 3). In models with sharp fault bends, it is necessary to round off the upper fault bend slightly in order to prevent problems with elemental collapse above the upper flat. In models with rounded fault bends, the maximum ramp dip, midway up the ramp, is 25°, and the lower and upper fault bends are circular arcs that meet at this midpoint.

3. Results

3.1. Elastic models

In order to investigate the stress field associated with different fault geometries, it is easier to observe a simple linear-elastic hanging wall subjected to small displacement, without the added complexity of plastic properties. We thus begin by investigating the stresses in an elastic hanging wall above faults with sharp or rounded fault bends. With sharp fault bends, both differential and mean stress are concentrated at the lower fault bend (Fig. 2). A steeply foreland-dipping lobe of high differential stress extends into the hanging wall from the fault bend. With an elastic–plastic material and greater fault displacement, this lobe will be the site of a backthrust shear band, propagating up from the lower fault bend. Mean stress is highest along the ramp, and there is low mean stress near the top surface above the ramp and immediately above the upper flat, regions that will become outer arcs of folds with greater fault displacement. With a stress-free top surface, these regions are in tension.

With rounded fault bends (Fig. 3), the highest mean stress is along the fault, midway up the ramp, instead of at the lower fault bend. Material above the lower fault bend is subjected to both low mean stress and low

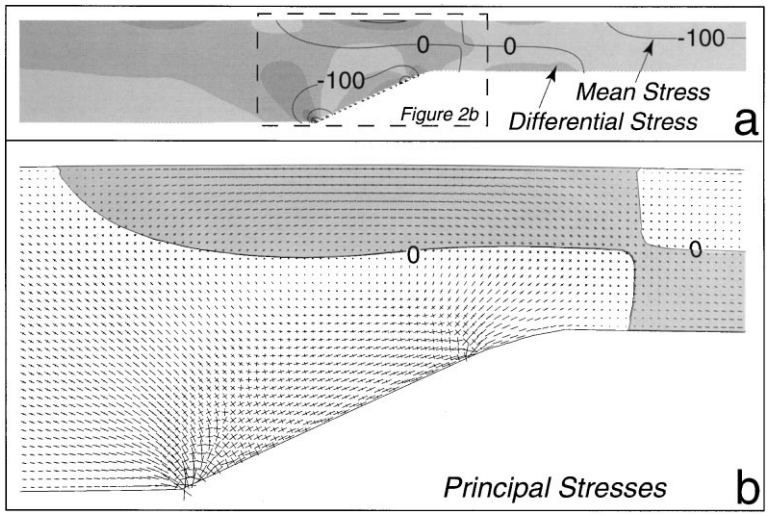

Fig. 2. Elastic model with sharp fault bends. (a) Differential stress (filled contours, contour interval = 100 MPa) and mean stress (black line contours, contour interval = 100 MPa). Dashed box shows region covered by Fig. 2b. (b) Principal-stress orientations. Gray region has positive (tensile) mean stress and, in this region, the long axes of principal stresses are tensile.

differential stress. Differential stress is highest at the upper fault bend along the fault, but there is also a local maximum above the lower fault bend near the middle of the layer. This maximum in differential stress at the middle of the layer, instead of at the base, will lead to bedding-parallel shear bands in the middle of an elastic–plastic layer, instead of backthrusts propagating from a stress concentration at a sharp lower fault bend. Principal-stress orientations in this elastic model are favorable for top-to-the-foreland shear sense above the lower fault bend, where they dip shallowly toward the foreland, and top-to-the-hinterland shear sense above the upper fault bend, where they dip shallowly toward the hinterland. The distributions of differential stress and mean stress and the orientations of principal stresses in these elastic models are similar to those in viscous analytical models with sharp or rounded fault bends (Kilsdonk and Fletcher, 1989).

3.2. Elastic–plastic models

Fault geometries in models with elastic–plastic hanging walls are the same as in the elastic models, either sharp or rounded. In elastic–plastic models with sharp fault bends, backthrusting dominates at the lower fault bend. As material moves over the lower fault bend, a backthrust propagates from the fault bend along the axial surface of the hanging-wall fold. Without cohesion softening, this backthrust is a zone of high shear-strain rate along the axial surface. Material moves through this zone of high shear-strain rate

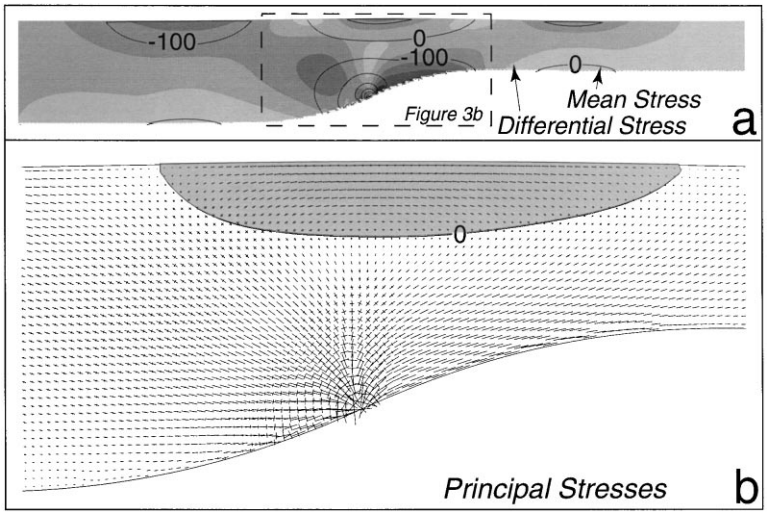

Fig. 3. Elastic model with rounded fault bends. (a) Differential stress (filled contours, contour interval = 100 MPa) and mean stress (black line contours, contour interval = 100 MPa). Dashed box shows region covered by Fig. 3b. (b) Principal-stress orientations. Gray region has positive (tensile) mean stress and, in this region, the long axes of principal stresses are tensile.

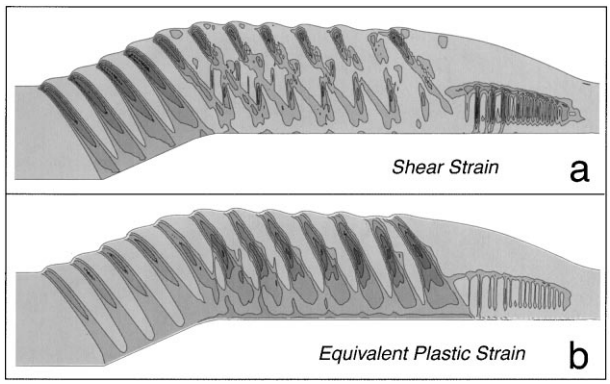

Fig. 4. Model with sharp fault bends and a stress-free top surface. (a) Shear strain (contour interval = 0.25) (b) Equivalent plastic strain (contour interval = 0.25).

to produce a uniform band of high shear strain above the ramp. With cohesion softening, strain localizes in the high strain-rate zone to produce a shear band. Because of the cohesion softening, the shear band becomes locked into the material and moves with it. The base of the shear band is pinned to the fault bend, but the shear band rotates to progressively steeper dips as material moves through the hinge (Erickson et al., in review). The shear band rotates until it reaches an unfavorable orientation with respect to the local stress field, at which point it is abandoned in favor of a new backthrust shear band, which propagates up from the fault bend. This initiation and abandonment of shear bands leads to a series of backthrust shear bands that are carried up the ramp (Fig. 4). These shear bands narrow upward, because of the rotation during their development. The strain within shear bands is greatest in the narrowest parts of shear bands near the top of the layer, and as a result, these are the locations of greatest cohesion softening. The softening law influences the spacing of backthrust shear bands and the amount of localization within them; a greater degree of softening leads to a wider spacing, because shear bands rotate farther before abandonment.

Before the first backthrust reaches the top of the ramp, deformation at the upper fault bend is fairly uniform, manifested primarily as vertical shear bands that are controlled by the mesh (Fig. 5b). The arrival of the backthrusts formed at the lower fault bend alters the deformation at the upper fault bend (Fig. 5c-e). Steeply-dipping to vertical shear bands continue to be active, and crosscut the existing backthrust shear bands. However, the backthrust shear bands are also reactivated as extension faults. The developing vertical shear bands curve into the existing shear bands at higher levels in the hanging wall, where localization is greatest in existing shear bands and where softening has produced the lowest cohesion. Because it is necessary to smooth the upper fault bend to prevent elemental collapse, deformation at the upper fault bend is not as localized as it might be with a sharper fault bend.

The reactivation of backthrusts as extension faults can be

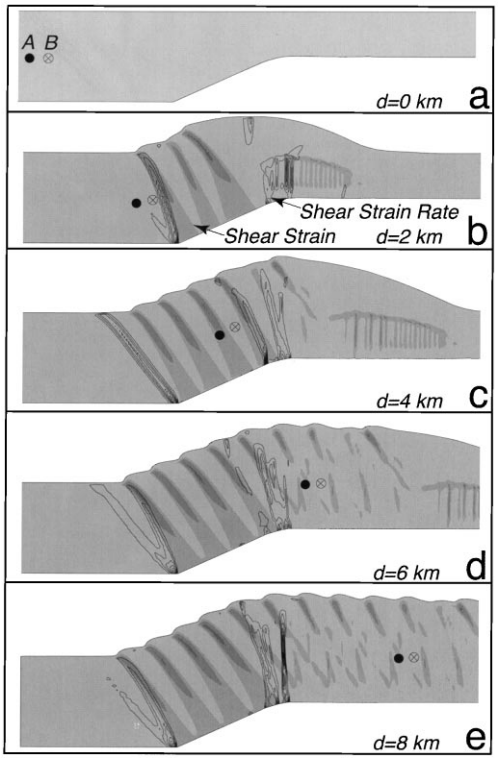

Fig. 5. Model with sharp fault bends and a stress-free top surface at five stages during its development. (a)–(e) are at displacements *d* of the left side of the model of 0, 2, 4, 6 and 8 km. Contours of shear strain (filled contours, CI = 0.4) and shear strain rate (black line contours, contour interval = 1×10^{-5}/timestep). Also shown are positions of two points, one of which (*A*) becomes incorporated into a backthrust shear band and another (*B*) that remains between backthrust shear bands (e.g. stage c). Stress paths for these points are shown in Fig. 13.

illustrated by comparing the distributions of two measures of strain (Fig. 4). Shear strain is a measure of the change in shape of each element relative to the initial state. On the other hand, equivalent plastic strain is a monotonically increasing function, and is a measure of accumulated material damage. Thus, if an element is strained to some state and then back to its initial state, the final shear strain will be zero, but the equivalent plastic strain will increase throughout the history. This type of strain history is essentially what happens in the models. As material passes over the lower fault bend, both the shear strain and equivalent plastic strain increase within shear bands. As these shear bands pass over the upper fault bend, the equivalent plastic strain increases but the shear strain decreases. Material is unstrained as it passes over the upper fault bend because backthrusts are reactivated as extension faults. The deformed grid also demonstrates the straining and unstraining related to reactivation (Fig. 6a, b). A shear strain is imparted on material in backthrust shear bands at the lower fault bend (Fig. 6a), which is partly removed as it passes over the upper fault bend (Fig. 6b). This result is similar to a model of Sanderson (1982) in which material moving over the upper fault bend undergoes an opposite

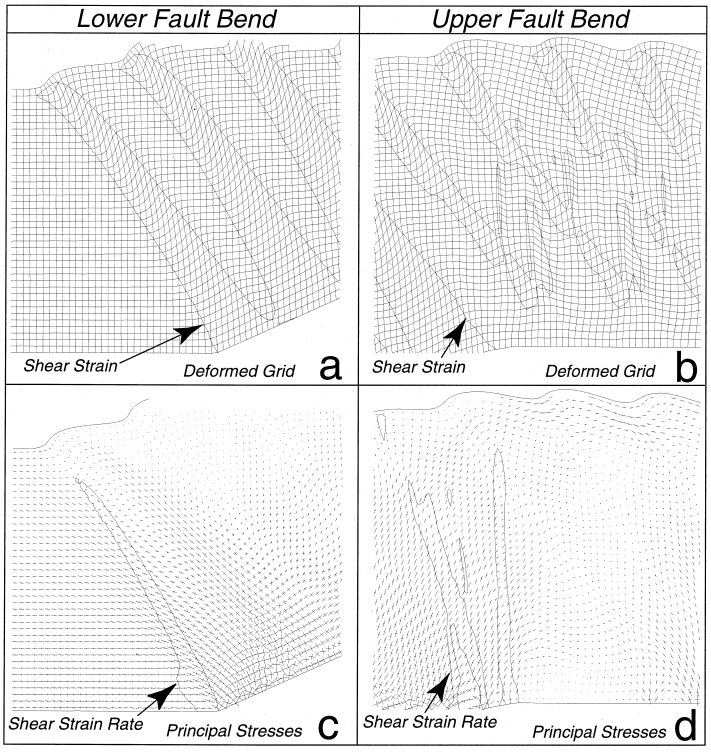

Fig. 6. Model with sharp fault bends and a stress-free top surface. Deformed grid and contour of shear strain = 0.4 at (a) the lower fault bend and (b) the upper fault bend. Principal-stress orientations and contour of shear strain rate = 2×10^{-5} /timestep at (c) the lower fault bend and (d) the upper fault bend.

sense of shear from that at the lower fault bend. Principal-stress orientations (Fig. 6c, d) indicate that the sense of shear within the shear bands reverses between the lower and upper fault bends, consistent with the switch from thrust faulting to extension faulting.

With rounded instead of sharp fault bends, bedding-parallel shear bands develop instead of backthrust shear bands at the lower fault bend. Without a sharp fault bend, there is no stress concentration at the hinge and instead there is a local maximum in differential stress in the middle of the layer (Fig. 3b). This stress distribution is consistent with Ramberg (1961) analysis of buckle folds, in which the shear strain is highest at the inflection point in the middle of the layer. It is also consistent with clay-cake models of buckle folds (Kuenen and de Sitter, 1938), in which bedding-parallel slip surfaces develop in the middle of layers at the inflection of limbs. As material passes over the lower fault bend, bedding-parallel shear bands develop with a top-to-the-foreland sense of shear (Fig. 7). The number and spacing of shear bands depends on fault geometry, material properties and layer thickness. These shear bands develop parallel to the grid, which introduces an anisotropy even if the material properties are isotropic. For example, with a grid oriented at 45° to vertical, these bedding-parallel shear bands do not develop (Erickson et al., in review). Thus, although the shear bands develop spontaneously, the slight anisotropy introduced by the grid enhances their development. The bedding-parallel shear bands are active in a region that is ~2 km wide parallel to the layer, as indicated by the distribution of shear-strain rate during their development (Fig. 8). Once the shear bands move past the lower fault bend and onto the ramp, they become inactive and are carried passively up the ramp.

At the upper fault bend, material undergoes a fairly uniform bedding-parallel extension during the early stages, before the shear bands that develop at the lower fault bend reach the upper fault bend. During this stage, there is no localization into shear bands at the upper fault bend. When the bedding-parallel shear bands reach the upper fault bend, they become reactivated, with a top-to-the-hinterland sense of slip. This reactivation leads to an increase in equivalent

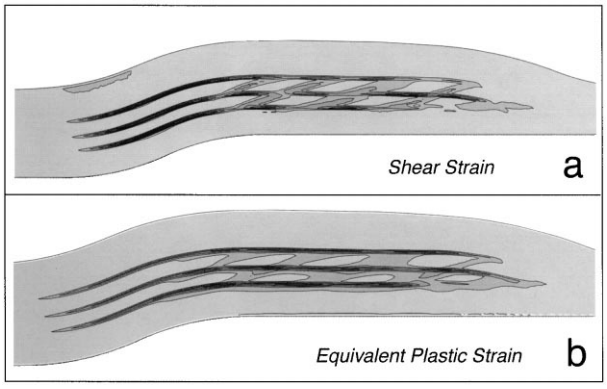

Fig. 7. Model with rounded fault bends and a stress-free top surface. (a) Shear strain (contour interval = 0.25). (b) Equivalent plastic strain (contour interval = 0.25).

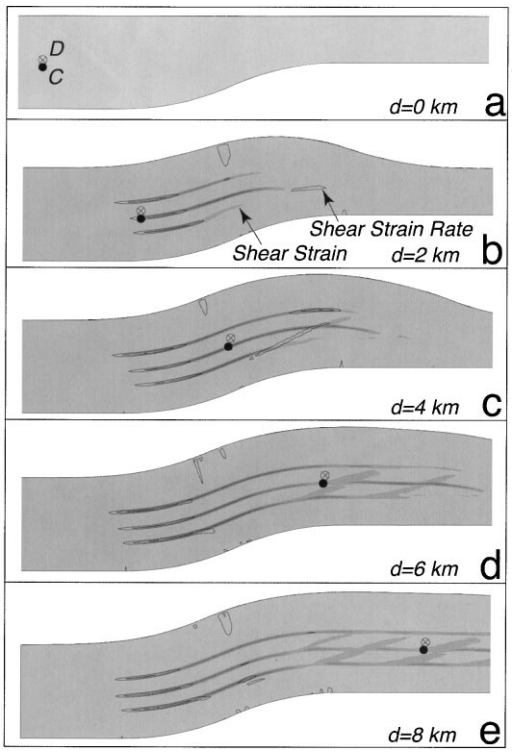

Fig. 8. Model with rounded fault bends and a stress-free top surface at five stages during its development. (a)–(e) are at displacements (d) of the left side of the model of 0, 2, 4, 6 and 8 km. Contours of shear strain (filled contours, contour interval = 0.4) and shear strain rate (black line contours, contour interval = 1×10^{-5}/timestep). Also shown are positions of two points, one of which (C) becomes incorporated in a bedding-parallel shear band and another (D) that remains between bedding-parallel shear bands. Stress paths for these points are shown in Fig. 14.

plastic strain within the shear bands and a concomitant decrease in shear strain within them (Fig. 7). This phenomenon is similar to that described above, in which material is unstrained back toward its initial state, with equivalent plastic strain monotonically increasing. In addition to this reactivation of the bedding-parallel shear bands, there are also newly-developed extensional shear bands that dip shallowly toward the hinterland. These extensional shear bands are listric into bedding-parallel shear bands and are active at the same time that the bedding-parallel shear bands are reactivated. The resulting structures are hinterland-verging extensional duplexes above the upper flat. The sense of shear in shear bands at the lower and upper fault bends can be seen in the deformed grid (Fig. 9). Shear bands develop with top-to-the-foreland shear sense at the lower fault bend and are unsheared by an opposite sense of shear at the upper fault bend. Cross-bedding shear bands are clearly extensional and down-to-the-hinterland.

Instead of relying on shear-band initiation to produce localized bedding-parallel shear, it is also possible to build bedding-parallel interfaces into the model (Fig. 10). A model with three bedding-parallel, frictionless interfaces in the hanging wall displays top-to-the-foreland slip on all three of the interfaces as they pass over the lower fault bend. Above the upper fault bend, the displacement on each interface is reduced, but not completely to zero, by top-to-the-hinterland slip. Top-to-the-foreland slip dominates, mainly because there is more shortening in the lower layers than in the upper layers, causing the upper layers to translate farther toward the foreland than the lower layers. There is only a small region of net top-to-the-hinterland slip, on the forelimb at the middle interface (Fig. 9b). In models in which bedding-parallel shear bands develop, similar shortening in lower layers causes shear bands to be only incompletely unsheared at the upper fault bend.

3.3. Ramp friction

In models with a frictionless fault and a sharp lower fault bend (Fig. 4), backthrusts develop with steep dips (~60°). These steep dips are in disagreement with physical models (Morse, 1977, 1978; Chester et al., 1991; Merle and Abidi, 1995), in which backthrusts dip ~35°. Increasing the friction on the ramp is one way to decrease the dip of shear bands into coincidence with the physical models, and is probably appropriate, because physical models have frictional interfaces. With the hanging-wall properties used here, high friction ($\mu = 0.36$) along the entire fault results

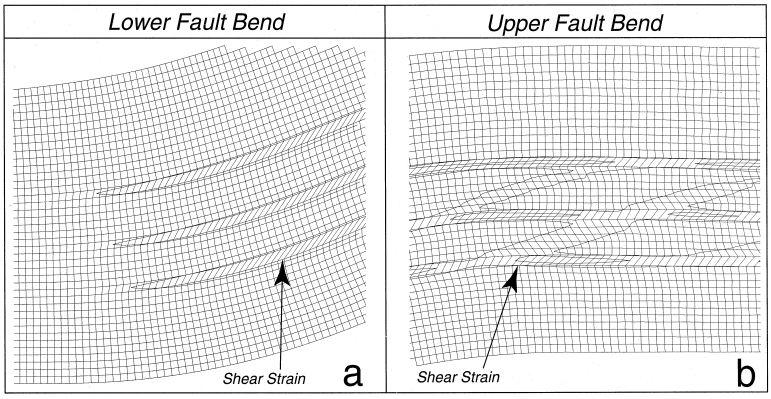

Fig. 9. Model with rounded fault bends and a stress-free top surface. Deformed grid and shear strain contours at (a) the lower fault bend (contour = 0.4) and (b) the upper fault bend (contours = 0.4, 0.8).

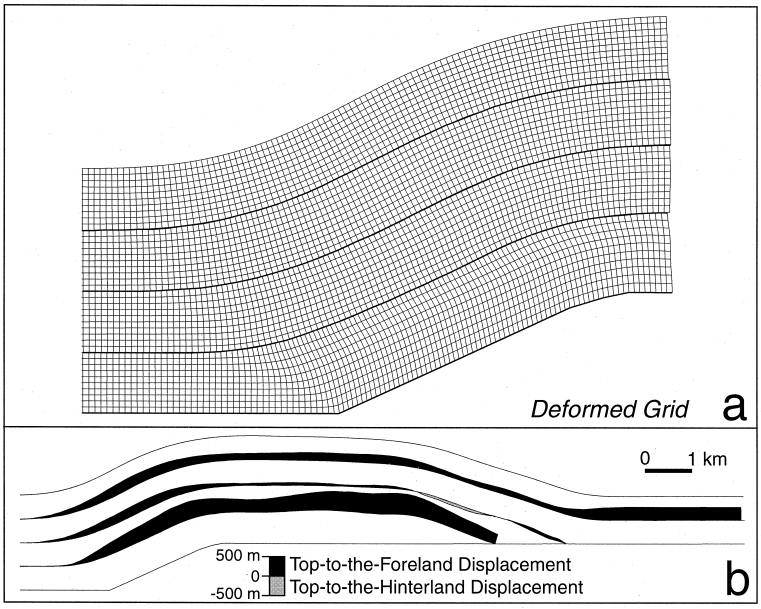

Fig. 10. Model with bedding interfaces. (a) Deformed grid. (b) Relative displacements on bedding-surface interfaces (black indicates top-to-the-foreland, gray indicates top-to-the-hinterland).

in the development of conjugate shear bands with thrust senses of shear above the lower flat, instead of movement of material up the ramp. High friction ($\mu = 0.36$) only along the ramp, with frictionless upper and lower flats and sharp fault bends, produces shallow-dipping (~39°) backthrusts at the lower fault bend (Fig. 11a; compare with Fig. 4a). The orientation of a shear band is determined by the orientation of the maximum principal stress (σ_1) and material properties (Vardoulakis, 1980). For a given set of material properties, the angle between a shear band and σ_1 is constant, and is 37.5° for the material properties used here. With friction on the ramp, σ_1 trajectories dip more shallowly (subhorizontally) because of the additional coupling between hanging-wall and footwall ramps. For a given set of hanging-wall material properties, the spacing of these backthrusts is similar to models with a frictionless fault and is not affected by friction on the fault; spacing is ~650 m with or without friction. With high friction ($\mu = 0.36$) on the ramp and with rounded fault bends (Fig. 11b), a conjugate set of backthrusts and shallow-dipping forethrusts develop at the lower fault bend, instead of the bedding-parallel shear bands that develop with a frictionless fault (Fig. 7a). The forethrusts are convex upward and shallow with increasing height in the hanging wall, although they never become parallel to bedding. In summary, friction on the ramp enhances backthrusting and causes backthrusts to form at shallower dips.

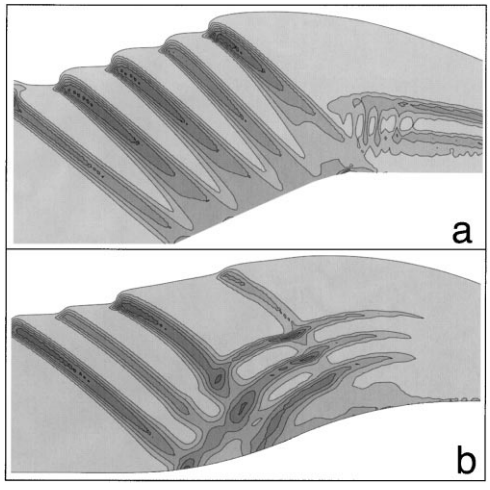

Fig. 11. Models with friction ($\mu = 0.36$) on the ramp (i.e. all parts of fault with dip >0°). Contours of shear strain (contour interval = 0.25). (a) Sharp fault bends. (b) Rounded fault bends.

3.4. Overburden

Adding a normal-stress boundary condition to the top surface of the layer simulates overburden. Normal stresses of 76.5 MPa and 133 MPa simulate overburdens of 3 km and 6 km, respectively. Because the strength of the material is pressure-dependent, an increase in overburden strengthens the material. Increased overburden also decreases the amount of localization, because an initially stronger material undergoes less strain and thus less cohesion softening. Shear bands are less well developed and more closely spaced with an increased overburden (Fig. 12). With a sharp fault bend, backthrust shear bands are spaced ~650 m with 0 km overburden (Fig. 4a), ~600 m with 3 km overburden (Fig. 12a), and there is little or no localization into shear bands with 6 km overburden (Fig. 12b). With increasing overburden, the maximum shear strain within shear bands decreases from 1.2 to 0.8 to 0.4 with 0, 3 and 6 km overburden. Because there is less cohesion softening

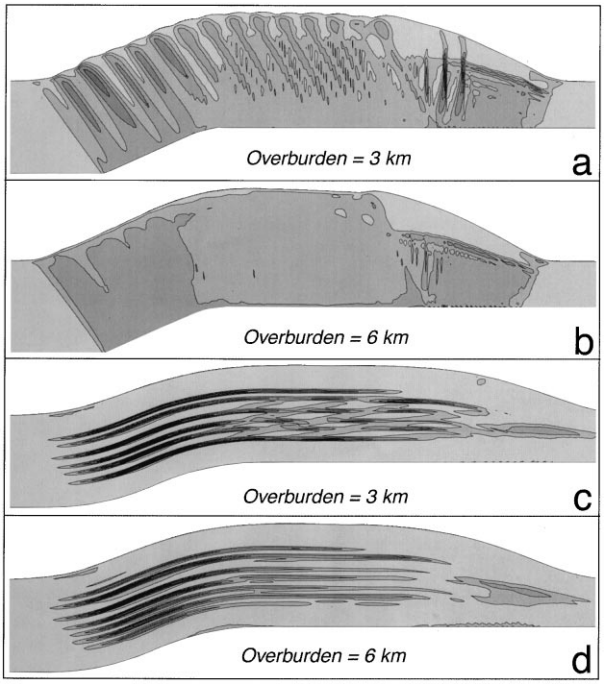

Fig. 12. Models with overburden, simulated by an applied normal traction on the top surface. See Figs. 4a and 7a for models with no overburden. Contours are of shear strain (contour interval = 0.2). (a) Sharp fault bends, 3 km overburden. (b) Sharp fault bends, 6 km overburden. (c) Rounded fault bends, 3 km overburden. (d) Rounded fault bends, 6 km overburden.

in each shear band, individual shear bands are active for a shorter time and rotate less with increasing overburden. Subvertical shear bands that develop at the upper fault bend are also more closely spaced with 3 km overburden than with 0 km, and become a fairly uniform distribution of shear strain with 6 km overburden. Similarly, with rounded fault bends (Fig. 7a, Fig. 12c, d), increasing overburden causes bedding-parallel shear bands to become more numerous (three with 0 km, six with 3 km, seven with 6 km) and more closely-spaced (on average, ~350 m with 0 km, ~200 m with 3 km, ~175 m with 6 km). Maximum shear strain in bedding-parallel shear bands decreases with increasing overburden (1.6 with 0 km, 1.2 with 3 km, 1.0 with 6 km). The hinterland-dipping extensional shear bands that develop at the upper fault bend with 0 km and 3 km overburden are absent with 6 km overburden. In summary, for both the sharp and rounded fault-bend geometries, the spacing of shear bands decreases and the amount of localization within them decreases with increasing overburden.

3.5. Stress paths of individual points

Tracking the stress history of individual points in a continuum can be a useful tool for understanding the mechanical evolution of a structure (Jamison, 1992). For each of the two models in Figs. 5 and 8, in which there is a stress-free top surface and either sharp or rounded fault bends, we follow two points as they move from the lower flat, over the ramp and onto the upper flat. One point in each model becomes incorporated in a shear band and the other point remains between shear bands. Stress paths plotted in principal-stress space demonstrate the stress and plastic-yield histories of each point. In these plots of principal-stress space (Figs. 13 and 14), mean stress increases to the upper right, whereas differential stress increases to the upper left. The initial yield surface, with cohesion 23 MPa, evolves with cohesion

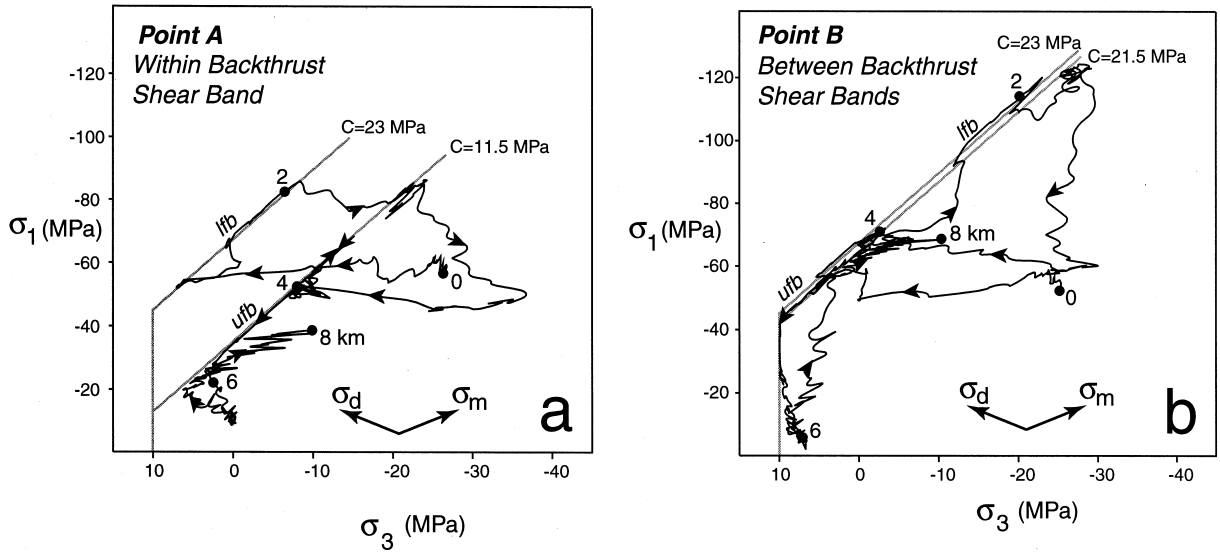

Fig. 13. Stress paths, in principal-stress (σ_1–σ_3) space, of two points in the model with sharp fault bends and stress-free top surface. Fig. 5 shows the positions of the points with time. (a) Stress path of point *A*. Also shown are the initial yield surface (cohesion = 23 MPa) and the yield surface at the maximum cohesion softening (cohesion = 11.5 MPa). (b) Stress path of point *B*. For this point, the yield surface at maximum softening has cohesion = 21.5 MPa. Axes of mean stress (σ_m) and differential stress (σ_d) are skewed because the σ_1 and σ_3 axes have different scales. Arrows show the evolution in time of the stress paths. Numbers on the paths represent the stress states at 0, 2, 4, 6 and 8 km of left-boundary displacement, and correspond to the stages in Fig. 5. *lfb* is lower fault bend, *ufb* is upper fault bend.

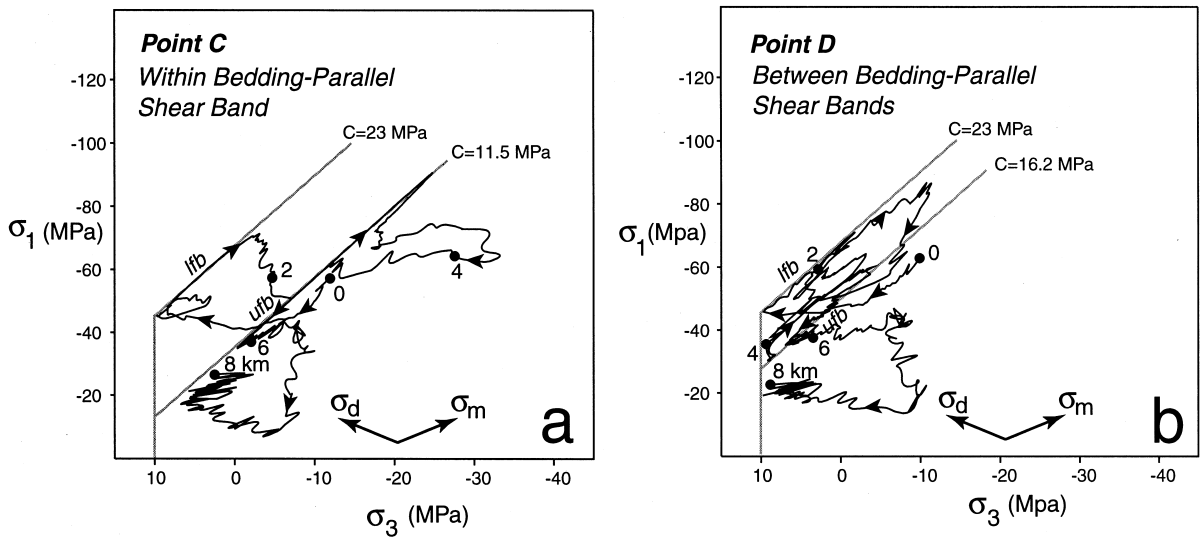

Fig. 14. Stress paths, in principal-stress space, of points in the model with rounded fault bends and free top surface. Fig. 8 shows the positions of the points with time. (a) Stress path of point *C*. Also shown is the initial yield surface (cohesion = 23 MPa) and the yield surface at the maximum cohesion softening (cohesion = 11.5 MPa). (b) Stress path of point *D*. For this point, the yield surface at maximum softening has cohesion = 16.2 MPa.

softening to lower differential stress values. The cohesion may soften to as much as 11.5 MPa at an equivalent plastic strain of 0.2, as defined by the softening law. The equivalent plastic strain and thus the cohesion and the yield surface vary in both space and time; each point's yield surface has a different history. Cohesion within shear bands softens to a minimum of 11.5 MPa, whereas cohesions outside of shear bands soften to some greater value because less strain accumulates. The tensile strength of 10 MPa places a tensional limit on the yield surface.

Stress histories are similar for the sharp fault-bend and rounded fault-bend models. Points that become incorporated in backthrust or bedding-parallel shear bands display similar stress paths (points *A* and *C*, Figs 13a, 14a). As the point moves toward the lower fault bend, differential stress increases until the stress state is on the yield surface ($d \sim 1.5$ km, Fig. 13a). The state of stress remains on the yield surface through the lower fault bend. As the point moves through the fault bend, the mean stress increases, because this is a region of layer-parallel shortening and compression. As strain accumulates in the shear band, the cohesion decreases and the yield surface evolves toward lower differential stress. As the point moves past the lower fault bend and onto the ramp, its state of stress falls below the yield surface because of decreasing differential stress. As the point moves onto the upper part of the ramp, mean stress decreases and differential stress increases, causing its stress path to change directions in principal stress space ($d \sim 3$ km, Fig. 13a). When the point reaches the upper fault bend ($d \sim 4$ km), the state of stress once again reaches the yield surface, which is now at its softened state. The mean stress continues to decrease as the stress path moves along the plastic yield surface and as the point moves through the upper fault bend. When the point reaches the upper flat ($d \sim 6$ km), the state of stress falls off the yield surface, because of a decrease in differential stress. Just past the upper fault bend, at a displacement of ~7 km, the state of stress is nearly isotropic, before returning to subvertical compression above the upper flat (Figs 6d, 13a). The stress paths of points in the backthrust (point *A*; Fig. 13a) and bedding-parallel (point *C*; Fig. 14a) shear bands are surprisingly similar as the shear bands localize at the lower fault bend, move up the ramp, and reactivate at the upper fault bend. The main difference between the two stress paths is that strain is more localized in the bedding-parallel shear bands, so that cohesion softens to the minimum sooner. Also, the stress path of the bedding-parallel shear band follows the softened yield surface for longer while going through the lower fault bend, because of the longer duration of deformation over a rounded fault bend relative to a sharp fault bend.

For points that are not within shear bands, the stress paths are similar to those described above, but because the points undergo less plastic strain, there is less cohesion softening of these points, as can be seen in the final yield surfaces (points *B* and *D*, Figs 13b, 14b). With the less-softened yield surface, the mean stress of these points continues to decrease as they reach the upper fault bend, producing some tensile failure as they intersect the yield surface at the tensile strength ($d \sim 5$ km, Fig. 13b). Also, the yield surface for these points softens through both lower and upper fault bends, because the minimum cohesion is never reached as it is within shear bands. For points that are between bedding-parallel shear bands but become part of an extensional shear band, the yield surface softens slightly through the lower fault bend, and then softens to the minimum cohesion within the extensional shear band at the upper fault bend.

Regardless of whether a point is in or out of a shear band, or the orientation of that shear band, the stress paths of all points have a generally similar form. The paths are also similar to those in models without cohesion softening (Erickson and Jamison, 1995; Strayer and Hudleston, 1997). There is an evolution of (1) increasing differential stress at the lower fault bend, (2) increasing mean stress along and then below the yield surface at the ramp, (3) increasing differential stress and decreasing mean stress along the yield surface at the upper fault bend, and (4) decreasing differential stress off the yield surface at the upper flat. Softening of the plastic yield surface causes the stress state to reach the yield surface sooner through the upper fault bend, for points within shear bands. This softening leads to a further concentration of strain in shear bands relative to surrounding material. The evolution of the yield surface by cohesion softening is thus a key factor in causing shear-band reactivation at the upper fault bend.

4. Discussion

Previous physical, analytical and numerical models of deformation at thrust-fault ramps (Morse, 1977; Berger and Johnson, 1980, 1982; Kilsdonk and Fletcher, 1989; Chester et al., 1991; Erickson and Jamison, 1995; Strayer and Hudleston, 1997) have produced generally similar results to those presented here, in spite of the different techniques and material properties used in each study. Stress distributions in analytical models (Berger and Johnson, 1982; Kilsdonk and Fletcher, 1989) are similar to those in our models (Figs. 2 and 3). Numerical modeling has an advantage over physical and analytical models because the effects of a variety of material and environmental parameters can be studied, because body forces can be included, and because realistic material properties can be used. The primary difference between this study and previous analytical and numerical modeling studies is that the use of an elastic–plastic, frictional, dilatant, cohesion-softening material and a fine mesh allow the development of shear bands. These shear bands simulate faults, and the cohesion softening simulates the weakening that occurs on faults. Cohesion softening enhances the development of shear bands and also increases the likelihood of reactivation of existing shear bands over the initiation of new ones at the upper fault bend. The formation of shear bands leads to deformation that more closely approximates deformation in natural upper crustal structures than previous analytical or numerical models.

Backthrusts are common features in physical models of deformation at thrust-fault ramps in which there is little or no material anisotropy and in which fault bends are sharp rather than rounded (Morse, 1977, 1978; Chester et al., 1991; Merle and Abidi, 1995). With an anisotropic material such as mica in the hanging wall, backthrusting is replaced by flexural-slip folding (Chester et al., 1991). In clay-cake models of buckle folds, bedding-parallel slip surfaces develop spontaneously (Kuenen and de Sitter, 1938). In our numerical models, as in the physical models, anisotropy determines whether backthrust or bedding-parallel shear bands develop. In addition, our models indicate that geometry and friction of the fault determine the importance of backthrusting versus flexural slip. Based on our results of the effects of fault geometry, listric faults should favor bedding-parallel slip, whereas stair-step faults should favor backthrusts in the hanging wall. However, listric faults are more likely to initiate in isotropic sequences, whereas stair-step faults are more likely to initiate in anisotropic sequences, and increased anisotropy favors bedding-parallel slip (Chester et al., 1991; Erickson et al., in review). Also, due to deformation at the ramp, fault bends may become more rounded with increasing displacement, causing a change from backthrusting to bedding-parallel slip. In order to reproduce the shallow dips of backthrusts in physical models, our numerical models must have a relatively high friction ($\mu = 0.36$) on the ramp, which is likely to approximate the conditions in physical models and possibly also on natural faults. High friction on the ramp causes maximum principal-stress orientations to be shallower because of the increased coupling between hanging wall and footwall across the ramp. Ramp angle has very little effect on backthrust shear-band orientation, especially for ramp angles of interest (20–30°) (Erickson et al., in review).

There have been several studies of deformation mechanisms in low-temperature sedimentary rocks that have moved over a thrust-fault ramp (Wiltschko et al., 1985; Kilsdonk and Wiltschko, 1988; Beutner et al., 1988; Srivastava and Engelder, 1990). Deformation mechanisms include faulting, extension fracturing, and pressure solution. Wiltschko et al. (1985) and Kilsdonk and Wiltschko (1988) studied the nature and sequence of deformation mechanisms in two regions of the Pine Mountain block of Tennessee. Wiltschko et al. (1985) observed early transport-perpendicular stylolites and later transport-perpendicular extension fractures, mesoscopic faults and bedding-surface slip. Kilsdonk and Wiltschko (1988) observed an early stage of mesoscopic thrust faults, transport-parallel extension fractures and transport-perpendicular stylolites, followed by a later stage of mesoscopic normal faults and transport-perpendicular extension fractures. Rocks in the Pennsylvania Valley and Ridge record layer-parallel extension by veins in the outer arcs of folds that developed over the lower and upper fault bends, and layer-parallel shortening by stylolites that developed over the ramp (Srivastava and Engelder, 1990). As in our numerical models with bedding-plane slip, multiple neutral surfaces developed in these folds. Beutner et al. (1988) studied cleavages and syntectonic fibers that record layer-parallel shortening over the lower flat, layer-parallel shortening and top-to-the-foreland shear at the lower fault bend, and then layer-parallel extension at the upper fault bend. All of these field studies indicate a general sequence of layer-parallel shortening at the lower fault bend followed

by layer-parallel extension at the upper fault bend. They also indicate layer-parallel shear and bending strains during movement over fault bends, as well as episodic and changing deformation mechanisms during movement over the ramp and fault bends. In all of these respects, the strain histories derived from field studies are consistent with our model results. Our models also predict stress paths of individual points in principal-stress space. These stress paths are similar with cohesion softening (this study) and without it (Erickson and Jamison, 1995; Strayer and Hudleston, 1997). Stress paths are useful for tracking the state of stress and yield surface of a point, but are difficult to test against present field data because magnitudes of stress are needed at different times for one point. However, with additional data near thrust-fault ramps, it may become possible to test the stress paths predicted by our models. Relations between a stress path and the yield surface also indicate stages when material undergoes plastic strain, which can be compared with sequences of fracture and faulting in natural structures (Erickson and Jamison, 1995).

Our models predict reactivation of mesoscopic faults as they move over the upper fault bend. This reactivation of mesoscopic faults may be difficult to recognize in the field, although multiple sets of slickensides are commonly observed on faults and bedding surfaces. Faults that have been reactivated with a sense of slip opposite to the original sense may have little or no final displacement. The hinterland-verging extensional duplexes that develop above the upper fault bend in the numerical models apparently have not been observed in natural structures. These extensional duplexes in the models look superficially like foreland-verging thrust duplexes, and natural examples could be misinterpreted as thrust duplexes without adequate information about slip on faults. Extensional faults are common features in the highly-deformed zones at the bases of thrust sheets (Wojtal, 1986; Erickson and Wiltschko, 1991) and foreland-verging extensional duplexes develop in these zones (Erickson, 1994). This extension at the bases of thrust sheets, which has been interpreted as the result of heterogeneous fault zone strength (Erickson and Wiltschko, 1991) or as a consequence of shear (Wojtal, 1992), might also be explained in some cases by movement over an upper fault bend. Large-scale, syn-thrust extension faults in the Moine thrust belt, which have been interpreted as analogous to surge zones in glaciers (Coward, 1982), may also be alternatively interpreted as having formed during movement over an upper fault bend.

5. Conclusions

We have used numerical continuum models with Mohr–Coulomb plasticity and cohesion softening to investigate the localization and reactivation of faults in the hanging wall of a thrust-fault ramp. In the models, deformation may localize as shear bands, which simulate faults. Material moving over the lower fault bend undergoes layer-parallel shortening and top-to-the-foreland shear, and backthrust shear bands or top-to-the-foreland, bedding-parallel shear bands form. Material moving over the upper fault bend undergoes layer-parallel extension and top-to-the-hinterland shear, and extensional shear bands or top-to-the-hinterland, bedding-parallel shear bands form. Which orientation of shear band dominates depends on fault geometry, fault friction, material properties and anisotropy. With a sharp lower fault bend, backthrust shear bands propagate up from the differential-stress concentration at the fault bend. With a rounded lower fault bend, bedding-parallel shear bands develop above the fault bend in the center of the layer, where differential stress is highest. Ramp friction enhances backthrusting, and produces shallower-dipping backthrusts. Increasing overburden decreases the localization in shear bands and the spacing between them. Shear bands that develop at the lower fault bend are weaker than the surrounding material and may be reactivated. Thus, the style of deformation at the upper fault bend depends on the deformation that accumulates at the lower fault bend. At the upper fault bend, backthrusts are reactivated as extension faults, and are crosscut by more steeply-dipping extension faults. Bedding-parallel shear bands are reactivated at the upper fault bend with top-to-the-hinterland sense of shear. Low-angle extension faults are listric into reactivated bedding-parallel shear bands, producing hinterland-verging extensional duplexes above the upper flat. Some of the features in the models (e.g. backthrusting and bedding-parallel slip, episodic shortening and extension) are also observed in natural structures and physical models. Other features (e.g. reactivated faults, hinterland-verging extensional duplexes) may be more difficult to recognize in the field. The models provide insight into the stress history and rock behavior during fault-bend folding, and serve as a predictive tool for the deformation mechanisms associated with fault-bend folds.

Acknowledgements

This paper benefited from the constructive reviews of Judith Chester and Olivier Merle. This research was funded by the members of the Princeton 3D Structure Project consortium: ARCO, Chevron, Elf, Intevep, Paradigm, Tarim, and Texaco.

References

Berger, P., Johnson, A.M., 1980. First-order analysis of deformation of a thrust sheet moving over a ramp. Tectonophysics 70, T9–T24.

Berger, P., Johnson, A.M., 1982. Folding of passive layers and forms of minor structures near terminations of blind thrust faults—application to the central Appalachian blind thrust. Journal of Structural Geology 4, 343–353.

Beutner, E.C., Fisher, D.M., Kirkpatrick, J.L., 1988. Kinematics of deformation at a thrust fault ramp (?) from syntectonic fibers in pressure shadows. In: Mitra, G., Wojtal, S.F. (Eds.), Geometries and

mechanisms of thrusting, with special reference to the Appalachians. Geological Society of America Special Paper 222, pp. 77–88.
Chester, J.S., Fletcher, R.C., 1997. Stress distribution and failure in anistropic rock near a bend on a weak fault. Journal of Geophysical Research 102, 693–708.
Chester, J.S., Logan, J.M., Spang, J.H., 1991. Influence of layering and boundary conditions on fault-bend and fault-propagation folding. Geological Society of America Bulletin 103, 1059–1072.
Coetzee, M.J., Hart, R.D., Varona, P.M., Cundall, P.A., 1995. FLAC Basics, Itasca Consulting Group, Minneapolis.
Coward, M., 1982. Surge zones in the Moine thrust zone of NW Scotland. Journal of Structural Geology 4, 247–256.
Cundall, P.A., 1989. Numerical experiments on localization in frictional materials. Ingenieur-Archiv 59, 148–159.
Cundall, P.A., 1990. Numerical modeling of jointed and faulted rock. In: Rossmanith, J. (Ed.), Mechanics of jointed and faulted rock, A. A. Balkema, Rotterdam, pp. 11–18.
Cundall, P.A., Board, M., 1988. A microcomputer program for modeling large-strain plasticity problems. In: Swoboda, C. (Ed.), Numerical Methods in Geomechanics. Proceedings of the 6th International Conference on Numerical Methods in Geomechanics, pp. 2101–2108.
Edmond, J.M., Paterson, M.S., 1972. Volume changes during the deformation of rocks at high pressures. International Journal of Rock Mechanics and Mining Science 8, 161–182.
Erickson, S.G., 1994. Deformation of shale and dolomite in the Lewis thrust fault zone, northwest Montana, USA. Canadian Journal of Earth Sciences 31, 1440–1448.
Erickson, S.G., Jamison, W.R., 1995. Viscous-plastic finite-element models of fault-bend folds. Journal of Structural Geology 17, 561–573.
Erickson, S.G., Strayer, L.M., Suppe, J., 2000. Numerical modeling of hinge-zone migration in fault-bend folds. Submitted to: McClay, K. (Ed.) Thrust Tectonics and Petroleum Systems.
Erickson, S.G., Wiltschko, D.V., 1991. Spatially heterogeneous strength in thrust fault zones. Journal of Geophysical Research 96, 8427–8439.
Hobbs, B.E., Ord, A., 1989. Numerical simulation of shear band formation in a frictional–dilational material. Ingenieur-Archiv 59, 209–220.
Jacobeen Jr., F., Kanes, W.H., 1974. Structure of the Broadtop syclinorium and its implications for Appalachian structural style. American Association of Petroleum Geologists Bulletin 58, 362–375.
Jamison, W.R., 1987. Geometric analysis of fold development in overthrust terranes. Journal of Structural Geology 9, 207–219.
Jamison, W.R., 1992. Stress spaces and stress paths. Journal of Structural Geology 14, 1111–1120.
Jamison, W.R., Pope, A., 1996. Geometry and evolution of a fault-bend fold: Mount Bertha anticline. Geological Society of America Bulletin 108, 208–224.
Kilsdonk, B., Fletcher, R.C., 1989. An analytical model of hanging-wall and footwall deformation at ramps on normal and thrust faults. Tectonophysics 163, 153–168.
Kilsdonk, B., Wiltschko, D.V., 1988. Deformation mechanisms in the southeastern ramp region of the Pine Mountain Block, Tennessee. Geological Society of America Bulletin 100, 653–664.
Kuenen, Ph.H., de Sitter, L.U., 1938. Experimental investigation into the mechanisms of folding, Leidsche Geologische Mededeelingen 10, 217–240.
Merle, O., Abidi, N., 1995. Approche éxperimentale du fonctionnement des rampes émergentes. Bulletin Societé de la Géologie Francaise 166, 439–450.
Morse, J., 1977. Deformation in ramp regions of overthrust faults: Experiments with small-scale rock models. Twenty-ninth annual field conference. Wyoming Geological Association Guidebook, pp. 457-470.
Morse, J., 1978. Deformation in ramp regions of thrust faults: Experiments with rock models. M.S. thesis, Texas A&M University.
Ord, A., 1991. Deformation of rock: A pressure-sensitive, dilatant material. Pure and Applied Geophysics 137, 337–366.
Ramberg, H., 1961. Relationship between concentric longitudinal strain and concentric shearing stain during folding of homogeneous sheets of rocks. American Journal Science 259, 382–390.
Rich, J.L., 1934. Mechanics of low-angle overthrust faulting illustrated by the Cumberland thrust block, Virginia, Kentucky and Tennessee. American Association of Petroleum Geologists Bulletin 18, 1584–1596.
Riley, D.J., 1996. Applications of numerical modeling to thrust tectonics. Ph.D. thesis, University of Southampton
Rudnicki, J.W., Rice, J.R., 1975. Conditions for the localization of deformation in pressure-sensitive dilatant materials. Journal of the Mechanics and Physics of Solids 23, 371–394.
Sanderson, D.J., 1982. Models of strain variation in nappes and thrust sheets: a review. Tectonophysics 88, 201–233.
Schultz, R.A., 1996. Relative scale and the strength and deformability of rock masses. Journal of Structural Geology 18, 1139–1149.
Serra, S., 1977. Styles of deformation in the ramp regions of overthrust faults. Twenty-ninth annual field conference. Wyoming Geological Association Guidebook, pp. 487–498.
Spang, J.H., Wolcott, T.L., Serra, S., 1981. Strain in the ramp regions of two minor thrusts, southern Canadian Rocky Mountains. In: Carter, N.L., Friedman, M., Logan, J.M., Stearns, D. (Eds.), Mechanical behavior of crustal rocks: The Handin volume. American Geophysical Union Geophysical Monograph 24, pp. 243–250.
Srivastava, D.C., Engelder, T., 1990. Crack-propagation sequence and pore-fluid conditions during fault-bend folding in the Appalachian Valley and Ridge, central Pennsylvania. Geological Society of America Bulletin 102, 116–128.
Strayer, L.M., Hudleston, P.J., 1997. Numerical modeling of fold initiation at thrust ramps. Journal of Structural Geology 19, 551–566.
Suppe, J., 1983. Geometry and kinematics of fault-bend folding. American Journal of Science 283, 684–721.
Vardoulakis, I., 1980. Shear band inclination and shear modulus of sand in biaxial tests. International Journal of Numerical and Analytical Methods in Geomechanics 4, 103–119.
Vermeer, P.A., de Borst, R., 1984. Non-associated plasticity for soils, concrete and rock. Heron 29, 1–64.
Wiltschko, D.V., 1979. A mechanical model for thrust sheet deformation at a ramp. Journal of Geophysical Research 84, 1091–1104.
Wiltschko, D.V., Medwedeff, D.A., Millson, H.E., 1985. Distribution and mechanisms of strain within rocks on the northwest ramp of Pine Mountain block, southern Appalachian foreland: a field test of theory. Geological Society of America Bulletin 96, 426–435.
Wojtal, S., 1986. Deformation within foreland thrust sheets by populations of minor faults. Journal of Structural Geology 8, 341–360.
Wojtal, S., 1992. Shortening and elongation of thrust zones within the Appalachian foreland fold–thrust belt. In: Mitra, S., Fisher, G.W. (Eds.), Structural geology of fold and thrust belts. Johns Hopkins University Press, pp. 93–103.